Joint structural and electrochemical modeling: Impact of porosity on lithium-ion battery performance

Vincent Laue [a, b], Fridolin Röder [a, b], Ulrike Krewer [a, b, *]

[a] *Institute of Energy and Process Systems Engineering, TU Braunschweig, Franz-Liszt-Strasse 35, Braunschweig, Germany*
[b] *Battery LabFactory Braunschweig (BLB), TU Braunschweig, Germany*

ABSTRACT

Future increases of energy density of lithium ion batteries require a systematic optimization of electrode structure and the related production process. Such optimization is facilitated by electrochemical models which predict cell performance with good accuracy. In this work, classic relations of structure to model parameters in the classical Doyle Newman electrode model are replaced to improve the prediction ac curacy of the model regarding electrode structure effects. Therefor, a 3D micro structure model is used to derive effective electrode property relations for ionic and electric conductivity, which are then used in the computationally efficient P2D framework of the Doyle Newman model. Simulations show clearly the transition from an electron transport limited to an ion transport limited electrode performance with increasing compression ratio. Integrating the derived algebraic structure model parameter relations into the electrochemical model allows a higher accuracy in predicting the optimal porosity of the experi mental data compared to the classical P2D model.

1. Introduction

Lithium ion batteries have outperformed other electrochemical storage technologies for more than twenty years. Just as the lithium ion battery is commonly found in all types of application, the pseudo two dimensional (P2D) battery model of Doyle et al. [1] has been commonly used in battery research and development for about 25 years. The homogenized model has proven its feasibility to reproduce the discharge behaviour of different cells in many publications [1—4]. However, the model is not feasible to reproduce many production effects such as calendering, i.e. compression of the electrode. Generally, in this work, the link between electrode structure parameters like porosity and model parameters like effective conductivity is referred to as structure model parameter relations. The probably most famous structure model parameter relation is the Bruggeman relation. In the calendering simulations published up to now, effective electrode parameters like conduc tivity and electrochemically active area, i.e. the material to electrolyte interface, have to be estimated for all calendering rates individually [2]. This allows a model based analysis of battery performance based on experimental data, but it causes the model's shortcomings in terms of prediction and optimization.

1.1. Calendering influence on cell performance

Calendering is the final step of electrode production before sheet separation, e.g. by cutting, and cell assembly. Together with coating and drying it is an important production step to influence micro structural properties of the electrodes and hence the cell performance. In principle, the calendering step is well understood. With increasing calendering rate, the electric conductivity in creases as the volume fraction of the conducting phase increases and a highly conductive network of conducting additives like Car bon Black or graphene is built. In contrast, calendering decreases the ionic conductivity of the electrode by decreasing the porosity. The optimal calendering rate would provide a trade off between both effects. For graphite anodes, this was shown e.g. by Shim and Striebel [5] and the negative effect of a too strongly compressed anode by Yang and Joo [6]. To understand the complex processes on micro scale in depth, research focused on different aspects. Beside the decrease of the electrode resistance due to the Carbon Black network, the contact resistance between active material and cur rent collector decreases significantly [7,8]. The influence of calen dering on pore size distribution and deformation of particles was

* Corresponding author. Battery LabFactory Braunschweig (BLB), TU Braunsch-weig, Germany.
E-mail address: u.krewer@tu-braunschweig.de (U. Krewer).

investigated by Haselrieder et al. [9]. Schmidt et al. investigated highly compressed NMC electrodes and found an optimal high current performance at moderate porosities and a maximal energy density at low porosities [10]. A too low compression can be detrimental compared to no calendering, as binder or Carbon Black bridges between particles can be fractured [9,11]. In addition, the calendering rate influences the wetting rate of the electrode which is important for the cell production planing and utilization of the active material. Experimental results of Sheng et al. showed an optimal wetting at moderate calendering [12].

1.2. Modeling calendering and structure effects

In terms of calendering, there are two different modeling approaches. On the one hand, there are process models to describe the production process itself. On the other hand, there are electrochemical models which are used to quantify the influence of calendering on the electrochemical cell performance.

Process models can be categorized into empiric models which are strongly related to experimental data [13], and highly sophisticated physics based models, e.g. based on the discrete element method (DEM). The physics based models simulate the particle movement during the calendering step to gain insight into processes as well as to determine the optimal calendering rate [14].

Electrochemical modeling is widely applied. However, only very few contributions are specifically assigned to calendering. Lenze et al. applied a P2D model to estimate the effective electrode properties at different calendering rates and revealed significant changes of electric conductivity and active surface area in dependence on the calendering rate [2]. Kenney et al. quantified the impact of deviations in the drying and calendering process, applying an electrochemical single particle model [15] and Smekens et al. simulated the calendering influence on a positive electrode [8].

Micro structures have been modeled frequently but mostly without focus on calendering. Some models are based on artificial structures [16–19], some reconstruct structures from e.g. FIB SEM images [20–24]. There are DEM micro structure models, e.g. see Ref. [25], FEM micro structure models, e.g. see Ref. [26], and full 3D electrochemical models [22,26–28]. The later suffer from excessive computational costs even at domain sizes of very few particle sizes [19]. Beside stochastic approaches and reconstruction, Liu and Mukherjee used a Kinetic Monte Carlo method to investigate the influence of solvent evaporation and interaction of solvent and nano particles on the conductive interfacial area [29]. Ngangdjong et al. introduced a multiscale approach of coarse grain molecule dynamic simulations coupled with a electrochemical full 3D model [30]. This approach allowed to predict the micro structure in dependence on the fabrication process and to simulate the electrochemical cell performance.

In electrochemical homogeneous models, structure model parameter relations provide the link between geometric structure properties like porosity and model parameters like effective ionic conductivity. In the classical Doyle Newman model three simplified structure model parameter relations are considered. For the effective ionic conductivity the Bruggeman relation is applied

$$\sigma_{\text{liq}} \quad \tilde{\sigma}_{\text{liq}} \cdot \varepsilon^{\beta} \tag{1}$$

which describes the influence of the porosity ε on the effective conductivity σ_{liq}. The Bruggeman coefficient β is a measure of tortuosity τ, as tortuosity can be determined by:

$$\tau \quad \varepsilon^{1-\beta}. \tag{2}$$

Thus, the bigger β the higher the tortuosity. For an electrode consisting of ideal spheres, β is equal to 1.5. In many publications, it is adjusted to fit simulated cell performance and experiments. In Eqs. (1) and (3), and in the further, a tilde denotes a bulk property.

For the electric conductivity, it is assumed:

$$\sigma_{\text{s}} \quad \tilde{\sigma}_{\text{AM}} \cdot \varepsilon_{\text{s}}^{\beta} \tag{3}$$

wherein ε_{s} is the solid phase volume fraction. In some publications the Bruggeman coefficient β is set to one for the solid phase [4] as the Bruggeman relation was developed only for the transport around spherical non contacting obstacles [31].

For the active surface area, which is the contact area between active material and electrolyte, the estimation

$$a_{\text{S}} \quad \frac{3 \cdot \varepsilon_{\text{S}}}{R_{\text{p}}} \tag{4}$$

is commonly known, which is based on the assumption of mono disperse particles of size R_{p} which do not contact each other. Independent on particle to particle contacts, the assumption of mono disperse spheres is limited by the densest possible particle packing of 74% solid.

In literature, various extended structure model parameter relations for conductivity exist. Zacharias et al. derived more accurate Bruggeman relations from experimental data for different porosities and Carbon Black amounts to enhance the accuracy of the effective ionic conductivity in an electrochemical battery model [32]. This approach is similar to the one presented in this article. Here however, a 3D model is used instead of experimental data, and further structural properties are investigated. Ott et al. introduced a micro mechanical model to derive effective ionic and electric conductivities of structures of mono disperse spherical [25]. This approach is similar to the micro structure model applied in this work. However, it neglects to consider the crucial impact of Carbon Black. Thus, no model based approach that considers structural impacts including Carbon Black on the LIB performance is available. The carbon black binder domain was considered by Ngandjong et al. in an electrochemical 3D model [30]. Compared to this model, our approach neglects concentration differences due to spatial effects, but the coupling approach with the P2D model allows optimization due to moderate computation costs. In the work of Bielefeld et al. the commercial software GeoDict was used [33]. The software allows automated generation of particle structures of different particle shapes and the article focused on the contact area of active material and electrolyte and the utilization fraction of active material. Derived percolation thresholds and active surface areas were in good accordance with results derived from the micro structure model in our previous study [34]. The major advantage of the self programmed micro structure model, compared to commercial software, is the flexibility with respect to novel focuses as well as the compatibility with the P2D model, which allows a fluent processing and optimization of batteries. In contrast to the work of Ngandjong et al. and Liu and Mukherjee [29,30], the applied model is limited to generic distributions, which is not governed by chemical processes in the drying step of the electrode production. Further, Carbon Black and binder are not distinguished. In this contribution we present a study on the crucial role of the spatial Carbon Black distribution on conductivity and active surface area to allow quantification and prediction of the calendering influence.

The outline of this work is as follows: First the micro structure model is introduced. From this, a set of algebraic structure model parameter relations is derived which is used to enhance the electrochemical model. Eventually, the feasibility of the framework of enhanced structure parameter relations and P2D model to

reproduce the experimental discharge curves for different calendering rates with a single parameter set is assessed.

This approach is chosen as results of Lenze et al. show that the homogeneous P2D model is able to simulate batteries at different calendering rates if the effective micro structure parameters are known for each calendering rate [2]. Hence, calendering rate dependent modeling of effective micro structure parameters allows an accurate prediction of cell performance at different calendering rates.

2. Cell setup and test conditions

For the electrochemical experiments a commercial three electrode setup was used. PAT Cells from the EL Cell GmbH provide a three electrode setup with a cylindrical electrode with a diameter of 18 mm and a separator with an included lithium reference electrode. The separator is a glass fiber separator by EL Cell GmbH (EU1 000210 0/X). For anode and cathode, graphite (SMG of Hitachi Corp.) and NMC 111 (BASF Corp.) were used, respectively. The paring of these electrodes was produced in the Battery Lab Factory Braunschweig on a pilot plant production line and were also studied in Refs. [14,35,36]. Ref. [14] provides further information on the respective compression forces of the different calendering rates and Ref. [35] provides details on the production process regarding e.g. the mixing process. Both electrodes had about 10 wt% of additives including Carbon Black and binder. The cathode was calendered to layer thicknesses of 82 μm, 70 μm, 64 μm, 62 μm, 59 μm and 55 μm while the anode was the same for all cells. The layer thickness of 82 μm represents the non calendered electrode. The porosity used in this work is a calculated one, based on measured weight (scales XS205, Mettler Toledo) and thickness (micrometer screw absolute digimatic IP66 of Mitutoyo) of the punched out electrodes. The electrolyte consists of EC, EMC and DMC with a ratio of 1:1:1 and traces of VC and CHB. For each cell 102.7 μL are used.

All experiments were conduced at 25°C in a temperature chamber. Discharge curves were recorded (Maccor 4000) between 4.2 V and 2.9 V.

3. Computational methods

The method applied in this work is illustrated in Fig. 1. Related to this, the structure generation and evaluation, the empiric surrogate models as well as the electrochemical model are introduced.

3.1. Micro structure generation and evaluation

The algorithms for the structure generation and evaluation have been published in Ref. [34] for a lithium based all solid state battery. Here, this approach is briefly summarized and modified to account for liquid electrolyte. Details are given in the appendix. General assumptions for the generated micro structure are as follows: homogeneous bulk within each phase, isotropic properties,

no structure changes along layer thickness, no breakage of AM and CB particles, no voids in the electrode.

As illustrated in Fig. 2, structure generation starts with setting randomly distributed nuclei with points $\zeta_{AM,i}$ in entire 3D domain for the active material phase AM. A nucleus fills the entire voxel. To every nucleus, a random numerical particle size $S_{AM,i} \in \mathbb{N}$ is assigned. Afterwards, nuclei for the Carbon Black binder phase at $\zeta_{CBM,i}$ are set. In contrast to AM nuclei, the nuclei at $\zeta_{CBM,i}$ are set in a sub domain, e.g. at the AM particle surface. To every $\zeta_{CBM,i}$ a random numerical particle size $S_{CBM,i}$ is assigned. Then, the domain of the electron conducting phase $\mathcal{M}_s$ and the domain of the ion conducting phase $\mathcal{M}_{liq}$, which is filled with liquid electrolyte, are set: Every voxel close to a AM nucleus becomes part of the AM particle, every voxel close to a CB nucleus becomes part of the CB domain if it is not part of the AM yet, and the remaining space is electrolyte.

To evaluate the effective electric and the ionic conductivity of the micro structure, the voxel based structure is transformed into a node based resistor network with the conductivity, wherein every node represents the center of a voxel. The connector conductivity between two nodes is dependent on size and bulk conductivity of the corresponding voxel. Considering one Dirichlet boundary condition of constant current and one Neumann boundary condition of constant potential allows to calculate the potential drop in the structure. From the macroscopic potential drop between the first and the last node, the effective conductivity can be determined This approach is applicable to the electron conducting phase, as well as to the ion conducting phase. To evaluate larger structures and to reduce stochastic effects, a super structure approach is applied wherein smaller evaluated structures become voxels of the super structure. For details and illustration see Ref. [34]. The volume specific active surface area a_S between active material and electrolyte is determined by counting electrolyte to AM interface areas.

In our previous work, numerical effects and deviations due to the randomness of the generation were addressed. Deviations of the predicted conductivity were generally below 5% and higher in the range of the percolation threshold of the CB network [34].

3.2. Electrochemical modeling

In this section, the electrochemical model is introduced which is based on the work of Legrand et al. [4]. The electrochemical model is extended with the enhanced structure model parameter relations derived in Section 4.2.

3.2.1. Governing equations

The P2D model of Doyle et al. [1] is based on a set of partial differential equations for the mass and charge balances of solid (Eqs. (5) and (6)), liquid (Eqs. (7) and (8)) and interfaces (Eqs. (9)–(11)). The most important equations are summarized in Table 1. For a complete list of symbols, it is referred to Table 7.

Cell voltage and half cell voltages are derived from the state variables. As the whole calendering influence shall be simulated
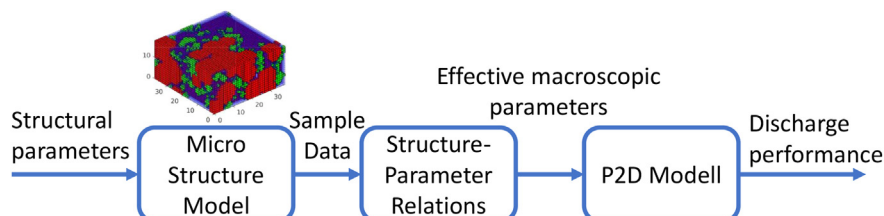

Fig. 1. Flow chart of the surrogate model approach: Sample structure generation/evaluation, ESMs and electrochemical simulations in P2D.
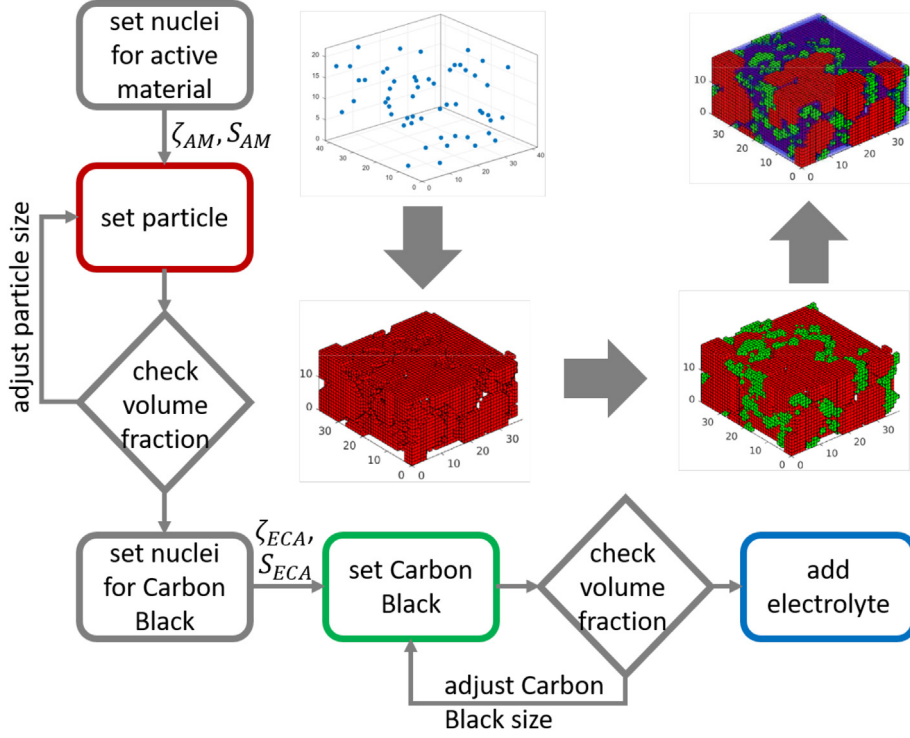
Fig. 2. Flow chart of the structure generation [34]. Randomly distributed nuclei (blue dots) are used to build up an electrode consisting of active material (red), Carbon Black (green) and electrolyte (blue). (For interpretation of the references to colour in this figure legend, the reader is referred to the Web version of this article.)

Table 1
Extract from the governing equations of the P2D standard model. For the full set of equations see Refs. [4,37]. L denotes the full cell thickness and $\delta_{e,a}$ and $\delta_{e,c}$ the layer thickness of anode and cathode, respectively.

Equations		Boundary Conditions	
$\dfrac{\partial c_s}{\partial t} = \dfrac{1}{r^2}\dfrac{\partial}{\partial r}\left(D_s r^2 \dfrac{\partial c_s}{\partial r}\right)$	(5)	$\dfrac{\partial c_s}{\partial r} = \dfrac{-j^{Li}}{z\,F\,a_s\,D_s},$ $r = R_p$	(12)
$j^{tot} = \dfrac{\partial}{\partial x}\left(\sigma_{s,eff}\dfrac{\partial \phi_s}{\partial x}\right)$	(6)	$\dfrac{\partial c_s}{\partial r} = 0, \; r = 0$	(13)
$\varepsilon\dfrac{\partial c_e}{\partial t} = \dfrac{\partial}{\partial x}\left(D_{e,eff}\dfrac{\partial c_e}{\partial x}\right)+(1-t_p)\dfrac{j^{Li}(x)}{F}$	(7)	$\dfrac{\partial c_e}{\partial x} = 0, \; x = \{0,\;L\}$	(14)
$j^{tot} = -\dfrac{\partial}{\partial x}\left(\sigma_{e,eff}\dfrac{\partial \phi_e}{\partial x}\right)$ $\quad -2\dfrac{RT}{F}(t_p-1)\sigma_{e,eff}\dfrac{\partial \ln c_e}{\partial x}$	(8)	$\dfrac{\partial \phi_s}{\partial x} = \dfrac{-I_{cell}}{A_{cell}\,\sigma_{s,eff}},$ $x = \{0,\;L\}$	(15)
$j^{tot} = j^{Li} + j^{DL}$	(9)	$\dfrac{\partial \phi_s}{\partial x} = 0,$ $x = \{\delta_{e,a},\; L-\delta_{e,c}\}$	(16)
$j^{Li} = a_s i_0\left(\exp\left(\alpha\dfrac{\eta F}{RT}\right)-\exp\left((\alpha-1)\dfrac{\eta F}{RT}\right)\right)$	(10)		
$i_0 = kF c_e^{\alpha}(c_{max}-c_s)^{\alpha}c_s^{1-\alpha}$	(11)	$\dfrac{\partial \phi_s}{\partial x} = 0, \; x = \{0,\;L\}$	(17)

with one parameter set, the extended model applies Eqs. (9b), (11) and (13), while the classical P2D model uses the structure parameter relations of Eqs. (1), (3) and (4). All other governing equations remain unchanged. For a complete list of e.g. geometric properties it is referred to Ref. [38].

3.2.2. Parameter estimation

In Section 4.3, parameters listed in Table 3 of the classical model and the extended model are estimated applying a curve fitting routine to discharge curves from 0.5C to 5C. As a three electrode setup was used in the experiments, half cell potentials of both electrodes are used.

For both models, exchange current densities, $i_{0,k}\,\forall k\in\{a,c\}$, and

Table 2
Parameter ranges of sample data for parameterization of the surrogate model.

Parameter	ε_{AM}	$\varepsilon_{CBM}/\varepsilon_{AM}$ ratio	σ_{CBM}/σ_{AM} ratio
lower bound	0.4	0	4810
upper bound	0.75	0.3	14286

solid phase diffusion coefficients $D_{s,k}\,\forall k\in\{a,c\}$, of both electrodes are derived from the experiments, as well as the diffusion coefficient of the electrolyte D_e. For the parameter estimation, values of $D_{s,k}$ etc. Taken from Ref. [38] are used as starting values. For the extended model, the bulk conductivity of NMC is derived from the experiments, while the conductivity of the Carbon Black binder

Table 3
Estimated parameters of the electrochemical model for different scenarios and models. $\overline{\sigma}_{c,CBM}$ 760 S m^{-1} [17].

Model	extended	classical	extended	extended
evaluated cells	all cells	all cells	cells 1 & 4	cells 1 & 6
parameter				
$D_{s,c}$ in m^{2}s^{-1}	4.976×10^{-12}	5.000×10^{-12}	4.976×10^{-12}	4.512×10^{-12}
$D_{s,a}$ in m^{2}s^{-1}	1.177×10^{-14}	11.097×10^{-14}	1.180×10^{-14}	0.879×10^{-14}
D_e in m^{2}s^{-1}	5.927×10^{-10}	6.693×10^{-10}	5.931×10^{-10}	6.058×10^{-10}
$\overline{\sigma}_{c,AM}$ in S m^{-1}	0.0161		0.0161	0.0167
$\overline{\sigma}_{s,AM+CBM}$ in S m^{-1}		0.0141		

matrix is kept constant at $\overline{\sigma}_{c,CBM}$ 760S m^{-1} [17]. For the classical model the solid phase bulk conductivity of the cathode is adjusted which does not distinguish between the contribution of active material and Carbon Black binder matrix. The anode conductivity is not adjusted since in literature a high conductivity of graphite electrodes is stated, e.g. 100S m^{-1} in Ref. [39].

The least square formulation for the parameter estimation is as follows

$$
\varepsilon(\Theta) \quad \sum_j \sum_k \sum_i \left(\left(\frac{U_{cell,sim,j,k}(\Theta, t_i) \quad U_{cell,exp,j,k}(t_i)}{U_{ref}} \right)^2 \right.
$$
$$
\left. + \quad \frac{\phi_{c,sim,j,k}(\Theta, t_i) \quad \phi_{c,exp,j,k}(t_i)}{U_{ref}} \right)^2 \right) \tag{5}
$$

wherein Θ is the parameter set and ε the cost function to minimize. The simulated cell voltage is $U_{cell,sim,j,k}(\Theta, t_i)$, and $\phi_{c,sim,j,k}(\Theta, t_i)$ is the simulated cathodic half cell potential at the C rate with index k and calendering rate with index j at the equidistant sample time t_i.

The parameter estimation routine leads to six adjustable parameters, which is comparable to published models, e.g. see Refs. [2,40]. Lenze et al. highlighted the different distinguishable influences of different parameters in C rate tests [2]. Further, Eq. (5) considers 4 C rates and 6 calendering rates simultaneously. This ensures uniqueness of the parameter set, as calendering has a characteristic influence on solid phase diffusion, surface over potential and electrolyte diffusion.

4. Results and discussion

In this section, micro structure simulations are presented and empiric surrogate models for the structure model parameter relations are derived from 3D simulations. Eventually, electro chemical simulation results are shown and validated with the experimental results of the calendering study to prove the concept of the enhanced structure model parameter from the micro structure model.

4.1. Micro structure modeling

In this section, different micro structures are investigated for a variation of porosity. All simulations are run with a constant volume ratio of 1/4.4 between the Carbon Black binder Matrix (CBM) and active material (AM) which is in accordance to the experimental cells in Section 2. Reference mean particle sizes of AM and CBM are 5.5 textmum and 1.83 textmum, respectively. The voxel size is 0.33 textmum. The CBM particle size represents agglomerates containing CB and binder. Related to Refs. [17,36,41], conductivities are assumed as follows: σ_{AM} 1.4×10^{-2}S m^{-1}, σ_{CB} 100S m^{-1} and σ_{ion} 0.6S m^{-1}. These values, are used to generate the samples for identification of the surrogate models. Literature values are used here, to ensure that the sample conductivity fit the

magnitude of the experimental conductivity. The exact conductivity of the materials are determined by parameter estimation as described in Section 3.2. Literature values can only provide a initial guess, as differences between different probes of the same material are large. For instance, for NMC conductivities are reported over three magnitudes [17,39,42].

In Fig. 3, the interface area between active material and electrolyte is shown for different porosities. As this work is related to calendering, all plots are plotted with decreasing porosity respectively increasing calendering rate from left to right. Calendering rate is initial (non calendered) layer thickness divided by layer thickness of the calendered electrode.

Blue dots represent the 3D simulations. The dashed line represents the widely used equation for active surface area, Eq. (4). At high porosities, surface area increases for the 3D structures as well as Eq. (4), as the number of particles increases and particle to particle contacts are marginal. The simulations show a maximal active surface area at a porosity of 0.45. At low porosities, the active surface area is decreased by particle particle contacts.

The influence of the electrode composition on electric and ionic conductivity is depicted in Fig. 4.

The simulated ionic conductivity (orange dots) decreases with decreasing porosity. The respective Bruggeman relation (orange dashed line) is in good accordance at high porosities. At low porosities, the simulated ionic conductivity decreases more significantly than the Bruggeman relation would assume, as first non connected pores occur, i.e. pores inactive for the macroscopic charge transport. Thus, there is a minimal porosity above zero, at which effective conductivity drops to zero. Calendering should stay well above this porosity.

The simulated electric conductivity (blue dots) increases slightly towards higher porosities, until at a porosity of about 0.35 the percolation of the Carbon Black network starts and the electric conductivity increases more significantly. The Bruggeman relation
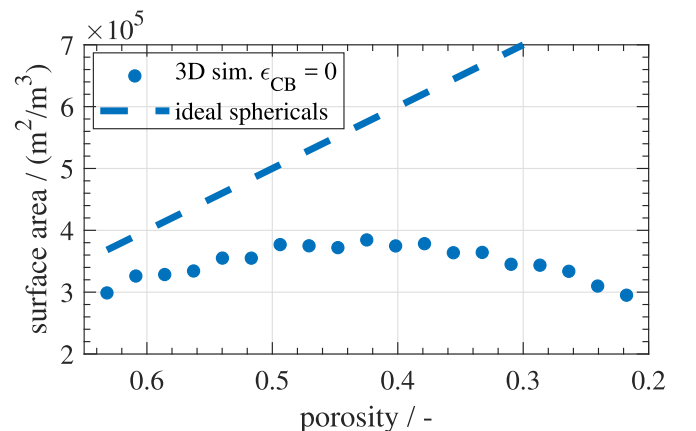

Fig. 3. Effective surface area vs. electrode porosity. 3D simulations are dots. Eq. (4) is the dashed line. Volume ratio between AM and CB is 1/4.4.
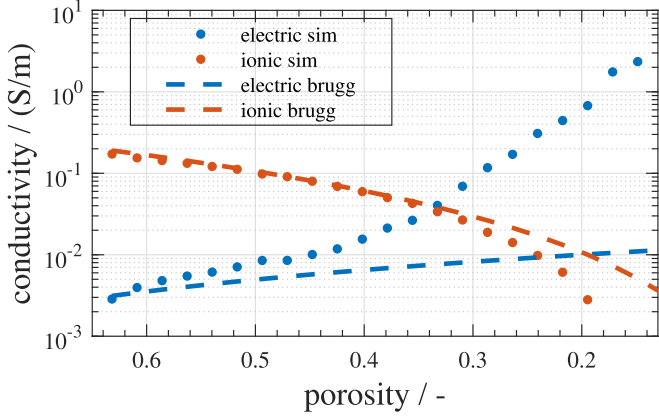
Fig. 4. Effective electric (blue) and ionic (orange) conductivity vs. porosity, resulting from 3D simulations (dots) vs. Bruggeman relations (dashed lines). Constant active material-to-Carbon Black volume ratio of 1/4.4. (For interpretation of the references to colour in this figure legend, the reader is referred to the Web version of this article.)

for the solid phase conductivity (blue dashed line) shows a small deviation at high porosities. At moderate to low porosities, the difference is several orders of magnitude, as the influence of the Carbon Black on the conductivity, which is neglected in the Bruggeman relation, is large. Thus, there is a percolation threshold above which Carbon Black forms a network containing only Carbon Black. This enables a high conductivity of the entire electrode.

As electric and ionic conductivity are both relevant for the discharge performance of a lithium ion battery, the intercept of electric and ionic conductivity in Fig. 4 could be a starting point to minimize the cell resistance and to maximize cell performance. Therefore, simulation results in Fig. 4 would suggest an optimal porosity of about 0.35. Applying the Bruggeman relation for electric and ionic conductivity would suggest an optimal porosity of 0.2 at a three times smaller conductivity. This highlights the importance of the usage of 3 dimensional models to obtain and understand effective conductivities, and to transfer this knowledge into electrochemical models.

4.2. Algebraic structure parameter relations

Structure model parameter relations applied in literature were reviewed in Section 1. In the following, based on structure simulations, three more accurate surrogates for those equations are derived: Eqs. (9b), (11) and (13). It should be noted that any type of surrogate model which fits the sample data could be used. Here, we try to stick to simple empiric equations which cover none the less essential physical effects as explained in the following.

For the further structure model parameter relations, effective volume fractions are introduced as part of the empiric surrogates:

$$\varepsilon_{AM}^* = \frac{\varepsilon_{AM} - \varepsilon_{crit,s}}{1 - \varepsilon_{crit,s}}, \quad \forall \varepsilon_{AM} : \varepsilon_{AM} > \varepsilon_{crit,s}, \tag{6}$$

$$\varepsilon^* = \frac{\varepsilon - \varepsilon_{crit,liq}}{1 - \varepsilon_{crit,liq}}, \quad \forall \varepsilon : \varepsilon > \varepsilon_{crit,liq}, \tag{7}$$

$$\varepsilon_{CBM}^* = \varepsilon_{CBM} \frac{\varepsilon_{CB} + \varepsilon_{AM} - \varepsilon_{crit,s}}{1 - \varepsilon_{crit,s}}, \quad \forall \varepsilon_{CBM} : \varepsilon_{CBM} + \varepsilon_{AM} > \varepsilon_{crit,s} \tag{8}$$

For electrolyte and AM the effective volume fractions represent the relative distance between the percolation threshold volume fraction of the individual phase and a volume fraction of one. Values range between zero and one. This allows to combine the simplicity of the Bruggeman relation with the existence of the percolation

threshold of the conducting network. The effective volume fractions of active material ε_{AM}^*, as well as the effective porosity ε^*, consider a critical percolation threshold of the conducting phase ε_{crit}, respectively for the solid and liquid phase: $\varepsilon_{crit,s}$ and $\varepsilon_{crit,liq}$. The volume fraction $\varepsilon_{crit,s}$ is related to the combined volume of AM and CBM. For the effective Carbon Black binder volume fraction ε_{CBM}^*, the strong interaction with the active material is additionally taken into account. Eq. (8) is equal ε_{CBM} for $\varepsilon_{CBM} = 1 - \varepsilon_{AM}$ and zero for $\varepsilon_{CBM} + \varepsilon_{AM} = \varepsilon_{crit,s}$. Thus, the effective volume fraction scales linearly between zero, at $\varepsilon_{crit,s}$, and the absolute volume fraction ε_{CBM}, where all voxels of one phase are connected. The difference between effective volume fraction of CBM and Eqs. (6) and (7) gives weight to the assumption that in a dense AM structure the CBM percolates at lower volume fractions than in a less dense AM structure. This can be expected as dense structures have lower active material surface areas [33,34], and thus, the CBM spreads to a smaller area. This leads to a higher surface area specific coverage of the AM with CBM and thus to a lower percolation threshold.

For the ion conducting phase, the Bruggeman relation is extended regarding the effects of percolation and Carbon Black. In addition, a nonzero critical percolation porosity $\varepsilon_{crit,liq}$ is considered in ε_{CBM}^* (see Eqs. (7) and (9a)) as well as an increase of tortuosity due to Carbon Black, represented by β_2 (see Eq. (9b)):

$$\sigma_{liq} = \tilde{\sigma}_{liq} \cdot (\varepsilon^*)^{\beta_1}, \sigma_{liq} = \tilde{\sigma}_{liq} \cdot (\varepsilon^*)^{\beta_1 + \beta_2}. \tag{9}$$

Eq. (9a), which is strongly related to Bruggeman, already provides a quite accurate fit, but for electrodes containing CBM Eq. (9b) outperforms it due to the additional empiric term β_2 which is:

$$\beta_2 = \varepsilon_{CBM}^{\nu_1} \tag{10}$$

Eq. (10) is related to an increase of liquid phase tortuosity due to Carbon Black, just as the Bruggeman coefficient for the active material phase. Due to that, Eq. (9b) is used in the further. The fitting parameters of these equations are $\varepsilon_{crit,liq}$, an exponent β_1 which is related to the tortuosity due to the active material like a Bruggeman coefficient and a second coefficient ν_1.

For the electron conducting phase, Eq. (11) is introduced, which consists of two summands. Due to the shape of the tangens hyperbolicus, the first summand is zero below the percolation threshold, is equal a Bruggeman type term, $\sigma_{CBM} \cdot (\varepsilon_{CBM}^*)^{\beta_3}$, representing the percolating CBM network above the percolation threshold, and has a steep transition between the both states. The mixed contribution of AM and CBM in the second summand can be understood as representation of a structure where CBM is present but does not form a network yet, but contribute to the AM network conductivity by e.g. connecting two AM particles. The mathematical formulation of the mixed contribution is related to a serial conduction of conducting AM element and a conducting AM element in parallel to a CBM element. This represents the physical processes in the electrode where the electron transport occurs partly in both materials, but the Carbon Black binder domain is not forming a matrix yet.

$$\sigma_s = \underbrace{\tilde{\sigma}_{CBM} \cdot (\varepsilon_{CBM}^*)^{\beta_3} \cdot \frac{1}{2} \left(1 + \tanh \left(\frac{1}{\nu_2} \varepsilon_{CBM}^* - \nu_3 \right) \right)}_{\text{contribution of percolated CB matrix}}$$
$$+ \left(\underbrace{\frac{1}{\tilde{\sigma}_{CBM} \cdot (\varepsilon_{CBM}^*)^{\beta_3} + 2\tilde{\sigma}_{AM} \cdot (\varepsilon_{AM}^*)^{\beta_4}}}_{\text{contribution of AM and non-percolated CBM}} + \underbrace{\frac{1}{2\tilde{\sigma}_{AM} \cdot (\varepsilon_{AM}^*)^{\beta_4}}}_{\text{AM contribution}} \right)^{-1}.$$
$$\tag{11}$$

The exponents β_3 and β_4 are related to the tortuosity of the two conducting materials and the coefficients ν_2 and ν_3 are dependent on the percolation threshold and the slope in the transition.

The fitting parameters are $\varepsilon_{\mathrm{crit,s}}$, β_3, β_4, ν_2, and ν_3. While Eq. (11) may seems quite long, for the absence of Carbon Black, it is equivalent to:

$$\sigma_{\mathrm{S}} \quad \tilde{\sigma}_{\mathrm{AM}} \cdot \left(\varepsilon_{\mathrm{AM}}^*\right)^{\beta_4} \tag{12}$$

For the effective surface area, Eq. (13) is introduced:

$$a_{\mathrm{S}} \quad \left(1 \quad \nu_4 \frac{\varepsilon_{\mathrm{CBM}}^{\nu_5}}{\varepsilon_{\mathrm{AM}}}\right) \nu_6 \frac{1 \quad 4(0.75 \quad \varepsilon_{\mathrm{AM}})^2 \cdot \varepsilon}{R_{\mathrm{p,AM}}} \tag{13}$$

The fitting parameters are ν_4, ν_5 and ν_6. The first term is related to the blocking of active material surface by Carbon Black which is dependent on the ratio of the two volume fractions. The bigger the volume fraction of CBM compared to AM, the less surface is accessible for electrolyte. The numerator of the second term is a downward parabola vs. $\varepsilon_{\mathrm{AM}}$ which takes into account that there is an increasing particle to particle contact area as well as less electrolyte with increasing volume fraction of active material. The denominator is the particle size, representing the influence of the particle size on the surface to volume ratio of particles just as in Eq. (4).

To derive algebraic structure model parameter relations, which in their entity are referred to as surrogate model, a set of sample structures is simulated applying the micro structure model. The different samples have varying electrode compositions and electric conductivities of Carbon Black. An excerpt of this data was presented above.

The ranges of the sample data are given in Table 2. Validity of surrogate model is only ensured for the sampled ranges. On the one hand, higher conductivity ratios can likely be calculated correctly as above a ratio of 14286 the physical process of percolation remains unchanged. On the other hand, the lower threshold is more relevant as below the bound, conduction through AM and conduction through CBM is not anymore as distinct as it is at high conductivity ratios. Exemplary fits of electric and ionic conductivity are shown in Figs. 5 and 6, respectively. They show percolation effects on the electric conductivity. The accordance for the ionic conductivity is higher than for the electric conductivity. This is related to the more complex processes for electrode conducting due to two conducting species compared to only on ion conducting species. Considering a smaller range of σ_{CBM} to σ_{AM} ratios would increase the accuracy of the fit for an individual σ_{CBM} to σ_{AM} ratio but would constrain the parameter range for the later parameter estimation.

Parameter estimation with the sample data leads to the parameters listed in Tables 4–6 for Eqs. (9b), (11) and (13).

4.3. Electrochemical modeling

In order to compare the electrochemical model with the derived new structure model parameter relations to the classical model, both are parameterized using the experimental discharge curves from the calendering study. It should be noted that the adjusted
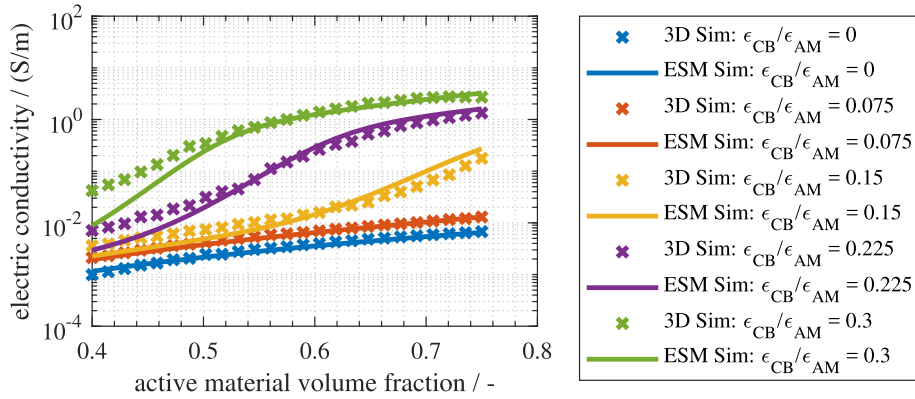

Fig. 5. Validation of surrogate model with 3D simulation data. Effective electric conductivity vs. active material volume fraction for various CBM contents for the 3D-simulations (crosses) and the surrogate model (lines) for σ_{CB} of 67.33 S m⁻¹ and σ_{AM} of 0.014 S m⁻¹.
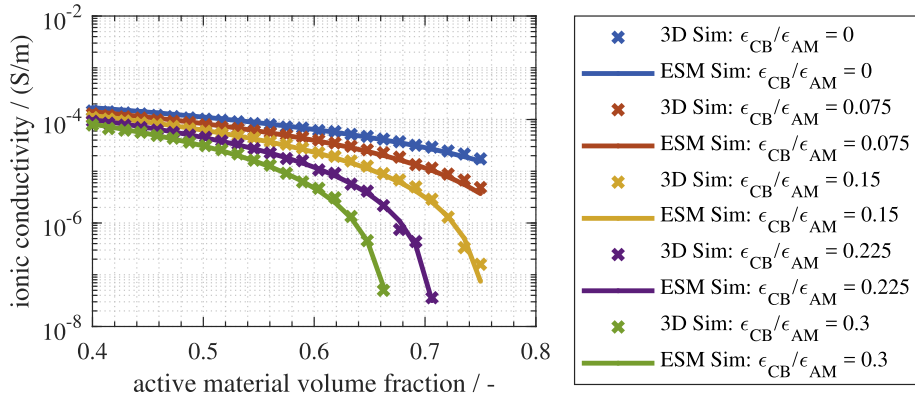

Fig. 6. Validation of surrogate model with 3D simulation data. Effective ionic conductivity vs. active material volume fraction for the 3D-simulations (crosses) and the surrogate model (lines) with an intrinsic ionic conductivity of.5 × 10⁻⁴ S m⁻¹.

Table 4
Parameters of Eq. (9b).

Parameter	$\varepsilon_{\text{crit.liq}}$	β_1	ν_1
Value	0.127	1.77	0.680

Table 5
Parameters of Eq. (11).

Parameter	$\varepsilon_{\text{crit.s}}$	β_3	β_4	ν_1	ν_2
Value	0.1	0.023	2.0	0.2	1.5

Table 6
Parameters of Eq. (13).

Parameter	ν_4	ν_5	ν_6
Value	0.904	1.127	4.912

Table 7
List of symbols.

Name	Symbol	Unit
active surface area	a_s	m^{-1}
Bruggeman coefficient	β	
cell area	A_{cell}	m^2
concentration	c	$\mathrm{mol\,m}^{-3}$
conductivity	σ	$\mathrm{S\,m}^{-1}$
current	I	A
current density	j	$\mathrm{A\,m}^{-2}$
diffusion coefficient	D	$\mathrm{m}^2\mathrm{s}^{-1}$
domain size	l	m
domain/set of voxel	Ω	
error	ε	
exchange current density	i_0	$\mathrm{A\,m}^{-2}$
Faraday constant	F	$\mathrm{A\,s\,mol}^{-1}$
geometric structure	$\mathcal{M}$	
ideal gas law constant	R	$\mathrm{J\,K}^{-1}\mathrm{mol}^{-1}$
layer thickness	δ_i	m
thickness of full cell	L	m
nucleus	ζ	
number of exchange electrons	z	
numerical parameter	ν	
numerical particle size	S	
overpotential	η	V
parameter set	Θ	
particle size	R_{p}	m
porosity	ε	
potential	ϕ	V
radius	r	m
reaction rate constant	k_i	s^{-1}
resistor network	$\mathscr{L}$	S
structure number of neighbors	$\mathscr{N}$	
time	t	s
transference number	t_{p}	
volume fraction	ε_i	
voxel edge length	Δx	m
voxel position	φ	

parameters consider all calendering rates simultaneously, consequently there are no individual parameter sets for different calendering rates. The parameter sets are provided in Table 3. In contrast to the novel approach introduced in this work, calendering simulations, e.g. by Lenze et al., used one parameter set per calendering rate [2].

The discharge capacities for different calendering rates from 0.2C to 5C and for varying porosity are depicted for the classical model in Fig. 7.
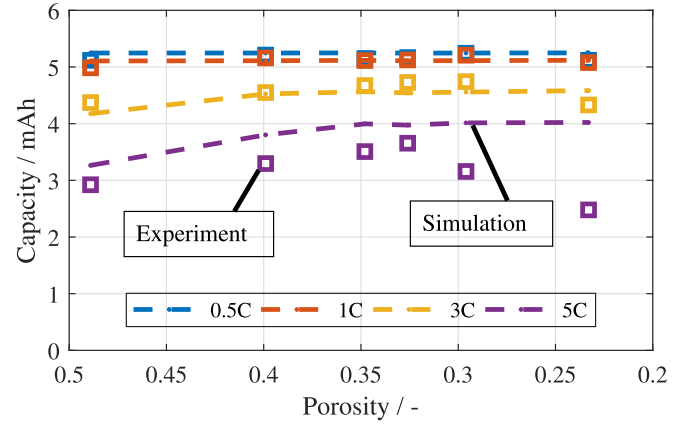

Fig. 7. Discharge capacity at 2.9 V for different C-rates in a calendering study with classical model (dashed lines) vs. experiment (squares) with a constant Carbon Black-to-active material volume ratio of 1/4.4.

Squares represent experimental data, dashed lines are simulations. Each column of squares in this plot represents one cell. From 0.5C to 1C, the experimental and simulated discharge capacities show no impact of the calendering rate. This is because, the discharge capacity is close to the theoretical capacity and is limited solely by solid phase diffusion. At 5C and high porosities the simulation reproduces the experiment, but at low porosities the simulated discharge capacity does not decrease, while the experimental capacity does. Hence, the classical model fundamentally fails to simulate the transition from an electrode limited due to poor electrical conductivity at high porosities to an electrode limited by poor ionic conductivity at low porosities.

In Fig. 8, the same experimental data are plotted together with the simulation results of the extended model.

At 0.5C and 1C also this model shows no influence of porosity on discharge capacity. For experiment and simulation, at 3C there is a slight and for 5C there is a distinct optimum of the discharge capacity at a porosity of about 0.35. The simulations reproduce experimental trends qualitatively nicely, though the capacity at 5C and 40% porosity is too high. Still, the experimental trend is correctly reproduced with the proposed model. Thus in contrast to the classical model, the extended model is feasible to simulate the transition from an electric conduction limited electrode to an ionic conduction limited electrode with increasing calendering rate.
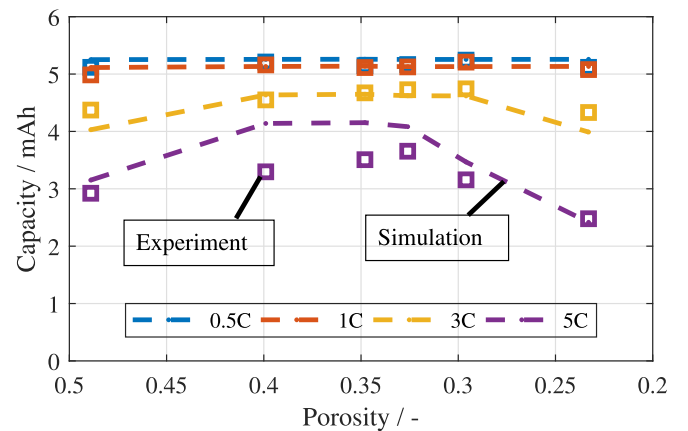

Fig. 8. Discharge capacity at 2.9 V for different C-rates in a calendering study with extended model (dashed lines) vs. experiment (squares) with a constant active material-to-Carbon Black volume ratio of 1/4.4.

Residuals of the parameter estimation of both models are depicted in Fig. 12 for quantitative comparison. The normalized residual of the extended model is about 9% lower than for the classical model.

In Figs. 9–11, discharge curves for the experiments and the extended model are shown for four C rates and 3 different calendering rate. For all C rates and calendering rates simulation and experiment are in good accordance, as well with respect to cell voltage, as with respect to half cell potential of the cathode. Thus, the extended model is feasible to predict the discharge performance as well as the overpotentials of the cell.

In conclusion, the extended model reproduces the calendering experiment while the classical model fails. From this, it is concluded that calendering effects are strongly related to change of porosity and the related conductivities and active surface area considered by the extended model. Further effects may occur due to surface resistance etc.

4.4. Evaluation of the robustness of the approach

In Section 4.3, all experimental data are used for the parameter
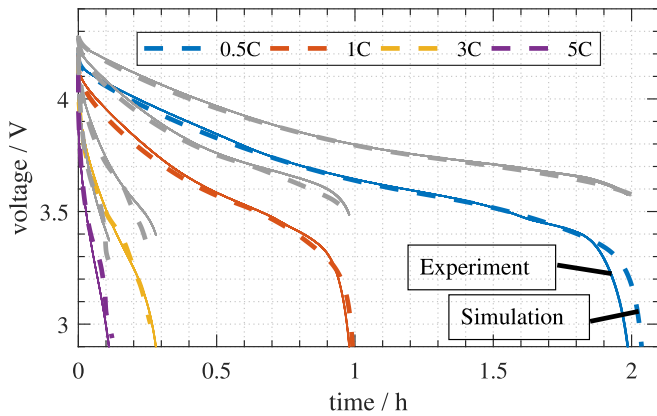

Fig. 9. Model validation with experimental data from a C-rate test in a three-electrode setup. Uncalendered cathode with a porosity of about 48.9% and an active material-to-Carbon Black-binder volume ratio of 1/4.4. Simulated (dashed lines) and experimental (solid lines) discharge curves. Gray lines represent the simulated (dashed lines) and experimental (solid lines) half-cell potential of the cathode. The extended model is used for simulations.
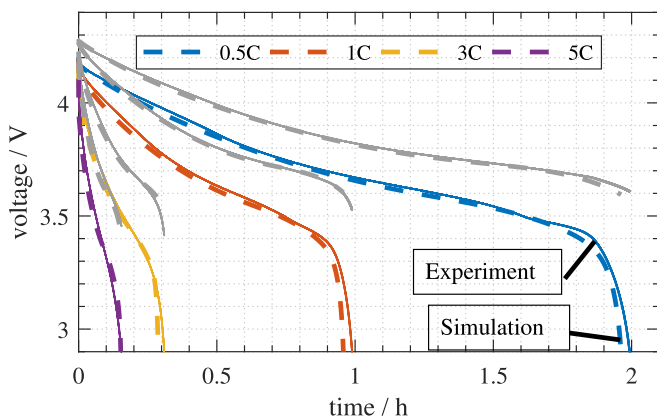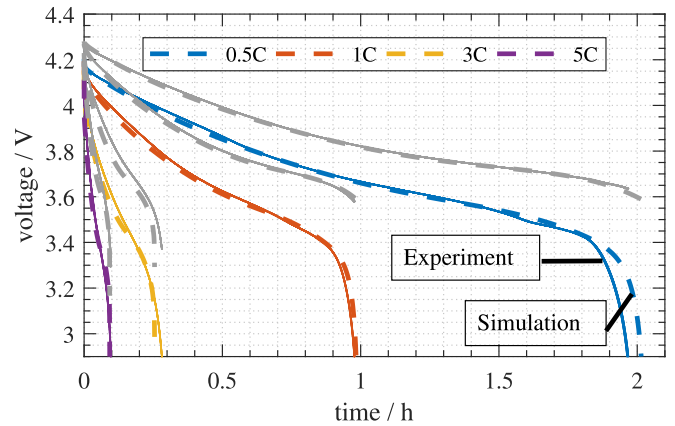

Fig. 10. Model validation with experimental data from a C-rate test in a three-electrode setup. Moderately calendered cathode with a porosity of about 32.6% and an active material-to-Carbon Black-binder volume ratio of 1/4.4. Simulated (dashed lines) and experimental (solid lines) discharge curves. Gray lines represent the simulated (dashed lines) and experimental (solid lines) half-cell potential of the cathode. The extended model is used for simulations.

Fig. 11. Model validation with experimental data from a C-rate test in a three-electrode setup. Highly calendered cathode with a porosity of about 23.3% and an active material-to-Carbon Black-binder volume ratio of 1/4.4. Simulated (dashed lines) and experimental (solid lines) discharge curves. Gray lines represent the simulated (dashed lines) and experimental (solid lines) half-cell potential of the cathode. The extended model is used for simulations.

estimation of the model. If the model shall be used for optimization of the calendering process, it has to be able to reproduce the experiment without using all presently available calendering data sets. To investigate the feasibility of the electrochemical model with the enhanced structure model parameter relations to predict the calendering impact properly, a scenario is assumed wherein only the non calendered cell and one single calendering rate is available. For this purpose, the parameter estimation and C rate test simulations from Section 4.3 are repeated for the extended model with the subset of data which consists of the non calendered cathode with a porosity of 48.9% and the cathode calendered to a layer thickness of 62 μm with a porosity of 32.6%, respectively uncalendered and highly calendered cell (23.3% porosity).

The estimated parameters are listed in Table 3 in comparison to those using the full data set and those using the classical model. Respective residuals are shown in Fig. 12. Consideration of the uncalendered and a moderately calendered cell leads to almost exact quantitatively the same parameters.

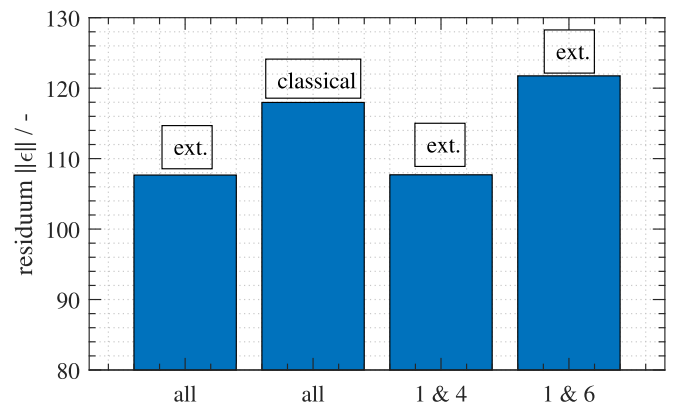Thus, even conducting only two experiments allow

Fig. 12. Residuals of the extended model (ext.) considering all cells for parameter estimation (PE), classical model considering all cells for PE, extended model considering an uncalendered and a moderately calendered cell (cells 1 & 4), and extended model considering an uncalendered and a highly calendered cell (cells 1 & 6). The residual is defined in Eq. (5) and is the sum of the squared deviation of cell voltage and cathode half-cell potential for all C-rates and all calendering rate, respectively, with 100 equidistant sample points per curve.

parameterization of the extended model and prediction of the optimal porosity with a precision of 5% points of porosity (see Fig. 8). Further experimental tests would be required to find the optimal calendering rate in this scenario as 5% points of porosity is not small compared to the parameter space. However, the model could reduce the total costs by reducing the number of required experiments in an combined experimental and simulation based optimization process compared to a solely experimental optimization.

There are different possible reasons of the discrepancy between measured and simulated discharge performance. In general, in fluences of the micro structure model, the surrogate model, the homogeneous model, as well as deviations in the experimental data are possible. The micro structure model provides an uncertain predictions of the effective parameters, as there is a discretization error, as well as there is a possible discrepancy between the real micro structure and the artificial structure which is evaluated. Lastly, the experimental data is based on cells with a diameter of 18 mm. Due to that, there could be an effect of manufacturing de viations on the cell properties. Electrodes were manufactured in a large scale role to role process. The length scale of process de viations are bigger than the cell size. The leads to possible cell to cell deviations.

Eventually, the estimated parameter set has to be unique, proving physical insight. The estimated parameters are in the of quantitative values provided in literature. Chen et al. reported a NMC bulk conductivity of 1.06×10^{-3} S m^{-1} and electrical con ductivity of the Carbon Black binder matrix of 760 S m^{-1}. For a slightly different electrolyte than applied here they stated a diffu sion coefficient of 1.2×10^{-9} m^{2}s^{-1} [17]. Vazquez Arenas et al. stated diffusion coefficients for graphite and NMC of 3.9×10^{-14} m^{2}s^{-1} and 1.64×10^{-14} m^{2}s^{-1}, respectively. The estimated parameters are in good accordance with the literature, while de viations are plausible since slightly different materials are used.

5. Conclusions

Accurate structure model parameter relations are essential for prediction and optimization of cell properties. This is especially important during electrode manufacturing, e.g. for the calendering process. Therefore, a 3D micro structure model was applied to derive more accurate structure model parameter relations than those applied in the classical Doyle Newman model. These include addition of Carbon Black and particle sizes and distributions. Arti ficial non spherical particles are generated in the micro structure model and the effective electric conductivity of an electrode, its ionic conductivity and interface area between active material and electrolyte are determined for various electrode compositions. Empirical surrogate models are derived from the conductivity re lations of the micro structure model and are used to extend the classical Doyle Newman model. The such extended electro chemical model is able to reproduce and predict the calendering experiment. A single experimental calendering rate allowed to estimate the optimal calendering rate with an accuracy of about 5% points. The feasibility of the extended model to reproduce the experiment suggests that homogeneous models could be sophis ticated enough to simulate the micro structure and calendering influence on the cell performance for the investigated system. For novel active materials, the approach should be validated again. Also, it is concluded that the investigated calendering rate primarily effects the porosity of the electrode. Consideration of effects like CB particle breaking or interface resistances were not required to predict the cell performance in dependence on the calendering rate.

In the further, the model may be applied to a wider range of electrode structure variations and to mathematically optimize electrode structure and calendering rate.

Appendix A. Micro Structure Generation and Evaluation

Consider a domain $\mathscr{M} \in \mathbb{N}^3$ which is our electrode. Any location in $\mathscr{M}$ is described by $\varphi \quad (x_1, x_2, x_3)^{\mathrm{T}}$. Any sub domain of $\mathscr{M}$ is denoted as Ω. Each structure consists of voxels of size $\Delta x \times \Delta x \times \Delta x$. For a complete list of symbols, it is referred to Table 7.

The structure generation starts with setting randomly distrib uted nuclei with points $\zeta_{\mathrm{AM},i}$ in entire $\mathscr{M}$ for the active material phase AM. To every nucleus a random numerical particle size $S_{\mathrm{AM},i} \in \mathbb{N}$ is assigned. The geometrical particle radius R_{p} can be derived from S by $R_{\mathrm{p}} \quad S \cdot \Delta x$. Afterwards, nuclei for the Carbon Black phase at $\zeta_{\mathrm{CB},i}$ are set. In contrast to AM nuclei, the nuclei at $\zeta_{\mathrm{CB},i}$ are set in a sub domain of $\mathscr{M}$ which is

$$\Omega_{\mathrm{CB}}^* \quad \{\varphi \in \mathscr{M} | \|\varphi \quad \zeta_{\mathrm{AM},i}\| > S_{\mathrm{AM},i} \; \forall i \wedge \mathscr{N}(\varphi) > 0\}, \tag{A.1}$$

wherein $\mathscr{N} \in \mathbb{N}^3$ is of the same size as $\mathscr{M}$ and contains the number of neighboring voxels containing active material for every voxel φ. To every $\zeta_{\mathrm{CB},i}$ a random numerical particle size $S_{\mathrm{CB},i}$ is assigned. Then, the domain of the electron conducting phase $\mathscr{M}_{\mathrm{s}}$ and the domain of the ion conducting phase $\mathscr{M}_{\mathrm{liq}}$, which is filled with liquid electrolyte, are set:

$$\mathscr{M}_{\mathrm{s}}(\varphi) \quad \begin{cases} 1 & \text{if } \exists \, \zeta_{\mathrm{AM},i} : \|\varphi \quad \zeta_{\mathrm{AM},i}\| \leq S_{\mathrm{AM},i} \; \forall i \\ 2 & \text{if } \exists \, \zeta_{\mathrm{CB},i} : \|\varphi \quad \zeta_{\mathrm{CB},i}\| \leq S_{\mathrm{CB},i} \; \forall i \\ & \wedge \nexists \, \zeta_{\mathrm{AM},i} : \|\varphi \quad \zeta_{\mathrm{AM},i}\| \leq S_{\mathrm{AM},i} \; \forall i \\ 0 & \text{else} \end{cases} \tag{A.2}$$

$$\mathscr{M}_{\mathrm{liq}}(\varphi) \quad \begin{cases} 1 & \text{if } \nexists \, \zeta_{\mathrm{CB},i} : \|\varphi \quad \zeta_{\mathrm{CB},i}\| \leq S_{\mathrm{CB},i} \; \forall i \\ & \wedge \nexists \, \zeta_{\mathrm{AM},i} : \|\varphi \quad \zeta_{\mathrm{AM},i}\| \leq S_{\mathrm{AM},i} \; \forall i \\ 0 & \text{else} \end{cases} \tag{A.3}$$

In Eqs. A.2 and A.3, the numbers 0, 1, 2, which are assigned to $\mathscr{M}_j \; \forall j \in \{\mathrm{s}, \mathrm{liq}\}$, are identifiers for the represented phases i.e. active material, carbon black and non conducting volume for $\mathscr{M}_{\mathrm{s}}$, respectively, and electrolyte and non conducting volume for $\mathscr{M}_{\mathrm{liq}}$, respectively. Eq. (A.3) is altered compared to Ref. [34], as voids in the liquid electrolyte are neglected here. Eqs. A.2 and A.3 describe the final structure that is generated. To get a structure which fits the set volume fractions, particles sizes S_{AM} and S_{CB} are adjusted iter atively. For details it is referred to Ref. [34].

To evaluate the effective electric conductivity of $\mathscr{M}_{\mathrm{s}}$ and the ionic conductive of $\mathscr{M}_{\mathrm{liq}}$, the voxel based structures $\mathscr{M} \in \mathbb{N}^3$ are transformed into a node based resistor network with the conduc tivity matrix $\mathscr{L} \in \mathbb{R}^2$. Introducing a connector conductivity $\mathscr{L}_{i,j}$ between nodes i and j in dependence on size and bulk conductivity of the corresponding voxel

$$\mathscr{L}_{i,j} \quad \tilde{\sigma}_{i,j} \cdot \Delta x_{\mathrm{voxel}}, \tag{A.4}$$

The resistor network becomes

$$\underline{\underline{\mathscr{L}}} \cdot \underline{\phi} = \underline{I} \tag{A.5}$$

wherein the vector $\underline{\phi}$ contains the potential in each node and the vector $\underline{I}$ the boundary currents. In this equation system, the first equation at $i = 1$ is a Dirichlet boundary condition of constant current I_{bc}.

$$\sum_{j=1}^{N} \mathscr{L}_{1j}(\phi_j - \phi_1) = I_{bc}. \tag{A.6}$$

The last equation at $i = N$ is a Neumann boundary condition of constant potential ϕ_{bc}.

$$(\phi_{bc} - \phi_N) = 0. \tag{A.7}$$

All intermediate equations, representing a individual connection between two nodes in the resistor network, are based on Ohm's law:

$$\sum_{j=1}^{N} \mathscr{L}_{i,j}(\phi_j - \phi_i) = 0, \ \forall i : \ 1 < i < N. \tag{A.8}$$

The first node and the last node are at opposite surfaces of the porous electrode structure, which allows to calculate the potential drop in the structure. For details and illustration see Ref. [34]. For the given boundary conditions, the current I_{bc} leaving the structure in node 1 and potential ϕ_{bc} in the last node, the potential in every node ϕ_i can be determined by solving Eq. (A.5). From the macroscopic potential drop between the first and the last node, the effective conductivity σ can be determined

$$\sigma = \frac{I_0 \cdot l}{\phi_N - \phi_1} \tag{A.9}$$

wherein l being the structure thickness.

The volume specific active surface area a_S between active material and electrolyte is determined by counting electrolyte to AM interface areas of size $\Delta x \times \Delta x$ in an structure of size $n_1 \times n_2 \times n_3$:

$$a_S = \frac{1}{n_1 n_2 n_3 \Delta x} \sum_{i=1}^{n_1} \sum_{j=1}^{n_2} \sum_{k=1}^{n_3} \begin{pmatrix} \mathscr{N}_{i,j,k} & \text{if } \mathscr{M}_{\text{liq},i,j,k} = 1 \\ 0 & \text{else} \end{pmatrix}. \tag{A.10}$$

References

[1] M. Doyle, Modeling of galvanostatic charge and discharge of the lithium/polymer/insertion cell, J. Electrochem. Soc. 140 (6) (1993) 1526, https://doi.org/10.1149/1.2221597.

[2] G. Lenze, F. Roder, H. Bockholt, W. Haselrieder, A. Kwade, U. Krewer, Simulation-supported analysis of calendering impacts on the performance of lithium-ion-batteries, J. Electrochem. Soc. 164 (6) (2017) A1223 A1233, https://doi.org/10.1149/2.1141706jes.

[3] N. Wolff, F. Roder, U. Krewer, Model based assessment of performance of lithium-ion batteries using single ion conducting electrolytes, Electrochim. Acta 284 (2018) 639 646, https://doi.org/10.1016/j.electacta.2018.07.125.

[4] N. Legrand, S. Rael, B. Knosp, M. Hinaje, P. Desprez, F. Lapicque, Including double-layer capacitance in lithium-ion battery models, J. Power Sources 251 (2014) 370 378, https://doi.org/10.1016/j.jpowsour.2013.11.044.

[5] J. Shim, K. Striebel, Effect of electrode density on cycle performance and irreversible capacity loss for natural graphite anode in lithium-ion batteries, J. Power Sources 119-121. doi:10.1016/S0378-7753(03)00235-0.

[6] G.F. Yang, S.K. Joo, Calendering effect on the electrochemical performances of the thick Li-ion battery electrodes using a three dimensional Ni alloy foam current collector, Electrochim. Acta 170 (2015) 263 268, https://doi.org/10.1016/j.electacta.2015.04.119.

[7] A. van Bommel, R. Divigalpitiya, Effect of calendering LiFePO4 electrodes, J. Electrochem. Soc. 159 (11) (2012) A1791 A1795, https://doi.org/10.1149/2.029211jes.

[8] J. Smekens, R. Gopalakrishnan, N. Steen, N. Omar, O. Hegazy, A. Hubin, J. Van Mierlo, Influence of electrode density on the performance of Li-ion batteries: Experimental and simulation results, Energies 9 (2) (2016) 104, https://doi.org/10.3390/en9020104.

[9] W. Haselrieder, S. Ivanov, H. Bockhold, A. Kwade, Impact of the calendering process on the interfacial structure and the related electrochemical performance of secondary lithium-ion batteries, ECS Trans. 50 (2013) 59 70, https://doi.org/10.1149/05026.0059ecst.

[10] D. Schmidt, M. Kamlah, V. Knoblauch, Highly densified ncm-cathodes for high energy li-ion batteries: Microstructural evolution during densification and its influence on the performance of the electrodes, J. Energy Storage 17 (2018) 213 223, https://doi.org/10.1016/j.est.2018.03.002.

[11] Z. Karkar, T. Jaouhari, A. Tranchot, D. Mazouzi, D. Guyomard, B. Lestriez, L. Roué, How silicon electrodes can be calendered without altering their mechanical strength and cycle life, J. Power Sources 371 (2017) 136 147.

[12] Y. Sheng, C.R. Fell, Y.K. Son, B.M. Metz, J. Jiang, B.C. Church, Effect of calendering on electrode wettability in lithium-ion batteries, Front. Energy Res. 2 (December) (2014) 1 8, https://doi.org/10.3389/fenrg.2014.00056.

[13] C. Meyer, M. Kosfeld, W. Haselrieder, A. Kwade, Process modeling of the electrode calendering of lithium-ion batteries regarding variation of cathode active materials and mass loadings, J. Energy Storage 18 (2018) 371 379, https://doi.org/10.1016/j.est.2018.05.018.

[14] C. Sangrós Giménez, B. Finke, C. Nowak, C. Schilde, A. Kwade, Structural and mechanical characterization of lithium-ion battery electrodes via DEM simulations, Adv. Powder Technol. 29 (2018) 2312 2321, https://doi.org/10.1016/j.apt.2018.05.014.

[15] B. Kenney, K. Darcovich, D.D. MacNeil, I.J. Davidson, Modelling the impact of variations in electrode manufacturing on lithium-ion battery modules, J. Power Sources 213 (2012) 391 401, https://doi.org/10.1016/j.powsour.2012.03.065.

[16] Y.-H. Chen, C.-W. Wang, G. Liu, X.-Y. Song, V.S. Battaglia, a. M. Sastry, Selection of conductive additives in Li-ion battery cathodes, J. Electrochem. Soc. 154 (10) (2007) A978, https://doi.org/10.1149/1.2767839.

[17] Y.H. Chen, C.W. Wang, X. Zhang, a. M. Sastry, Porous cathode optimization for lithium cells: Ionic and electronic conductivity, capacity, and selection of materials, J. Power Sources 195 (9) (2010) 2851 2862, https://doi.org/10.1016/j.jpowsour.2009.11.044.

[18] M.M. Forouzan, C.W. Chao, D. Bustamante, B. Mazzeo, D.R. Wheeler, Experiment and simulation of the fabrication process of lithium-ion battery cathodes for determining microstructure and mechanical properties, J. Power Sources 312 (2016) 172 183, https://doi.org/10.1016/j.jpowsour.2016.02.014.

[19] C.-W. Wang, A.M. Sastry, Mesoscale modeling of a Li-ion polymer cell, J. Electrochem. Soc. 154 (11) (2007) A1035, https://doi.org/10.1149/1.2778285.

[20] G. Inoue, M. Kawase, Numerical and experimental evaluation of the relationship between porous electrode structure and effective conductivity of ions and electrons in lithium-ion batteries, J. Power Sources 342 (2017) 476 488, https://doi.org/10.1016/j.jpowsour.2016.12.098.

[21] A. Etiemble, N. Besnard, A. Bonnin, J. Adrien, T. Douillard, P. Tran-Van, L. Gautier, J.C. Badot, E. Maire, B. Lestriez, Multiscale morphological characterization of process induced heterogeneities in blended positive electrodes for lithium ion batteries, J. Mater. Sci. 52 (7) (2017) 3576 3596, https://doi.org/10.1007/s10853-016-0374-x, arXiv:1512.00567.

[22] T. Danner, M. Singh, S. Hein, J. Kaiser, H. Hahn, A. Latz, Thick electrodes for Li-ion batteries: A model based analysis, J. Power Sources 334 (2016) 191 201, https://doi.org/10.1016/j.jpowsour.2016.09.143.

[23] T. Carraro, J. Joos, B. Rüger, A. Weber, E. Ivers-Tiffée, 3D finite element model for reconstructed mixed-conducting cathodes: I. Performance quantification, Electrochim. Acta 77 (2012) 315 323, https://doi.org/10.1016/j.electacta.2012.04.109. URL, https://doi.org/10.1016/j.electacta.2012.04.109.

[24] M. Ender, J. Joos, T. Carraro, E. Ivers-Tiffee, Quantitative characterization of LiFePO4 cathodes reconstructed by FIB/SEM tomography, J. Electrochem. Soc. 159 (7) (2012) A972 A980, https://doi.org/10.1149/2.033207jes. URL, http://jes.ecsdl.org/cgi/doi/10.1149/2.033207jes.

[25] J. Ott, B. Volker, Y. Gan, R. McMeeking, M. Kamlah, A micromechanical model for effective conductivity in granular electrode structures, Acta Mech. Sin. 29 (2013) 682 698, https://doi.org/10.1007/s10409-013-0070-x.

[26] S. Hein, J. Feinauer, D. Westhoff, I. Manke, V. Schmidt, A. Latz, Stochastic microstructure modeling and electrochemical simulation of lithium-ion cell anodes in 3D, J. Power Sources 336 (2016) 161 171, https://doi.org/10.1016/j.jpowsour.2016.10.057.

[27] D. Westhoff, J. Feinauer, K. Kuchler, T. Mitsch, I. Manke, S. Hein, A. Latz, V. Schmidt, Parametric stochastic 3D model for the microstructure of anodes in lithium-ion power cells, Comput. Mater. Sci. 126 (2017) 453 467, https://doi.org/10.1016/j.commatsci.2016.09.006.

[28] C.-F. Chen, A. Verma, P.P. Mukherjee, Probing the role of electrode microstructure in the lithium-ion battery thermal behavior, J. Electrochem. Soc. 164 (11) (2017) E3146 E3158, https://doi.org/10.1149/2.0161711jes.

[29] Z. Liu, P.P. Mukherjee, Microstructure evolution in lithium-ion battery electrode processing, J. Electrochem. Soc. 161 (8) (2014) E3248 E3258, https://doi.org/10.1149/2.026408jes. URL, http://jes.ecsdl.org/lookup/doi/10.1149/2.026408jes.

[30] A.C. Ngandjong, A. Rucci, M. Maiza, G. Shukla, J. Vazquez-Arenas, A.A. Franco, Multiscale simulation platform linking lithium ion battery electrode fabrication process with performance at the cell level, J. Phys. Chem. Lett. 8 (23)

(2017) 5966 5972, https://doi.org/10.1021/acs.jpclett.7b02647.

[31] A. Vadakkepatt, B. Trembacki, S. Mathur, J. Murthy, Bruggeman's exponents for effective thermal conductivity of lithium-ion battery electrodes, J. Electrochem. Soc. 163 (2) (2016) A119 A130, https://doi.org/10.1149/2.0151602jes.

[32] N. Zacharias, D.R. Nevers, C. Skelton, K. Knackstedt, D.E. Stephenson, D.R. Wheeler, Direct measurements of effective ionic transport in porous Li-ion electrodes, J. Electrochem. Soc. 160 (2) (2013) A306 A311, https://doi.org/10.1149/2.062302jes.

[33] A. Bielefeld, D. a. Weber, J. Janek, Microstructural modeling of composite cathodes for all-solid-state batteries, J. Phys. Chem. C 123 (3) (2019) 1626 1634, https://doi.org/10.1021/acs.jpcc.8b11043.

[34] V. Laue, N. Wolff, F. Roder, U. Krewer, Modeling the influence of mixing strategies on micro structural properties of all-solid state electrodes, Energy Technol.. doi:10.1002/ente.201801049. URL http://doi.wiley.com/10.1002/ente.201801049.

[35] H. Dreger, W. Haselrieder, A. Kwade, Influence of dispersing by extrusion and calendering on the performance of lithium-ion battery electrodes, J. Energy Storage 21 (2019) 231 240, https://doi.org/10.1016/j.est.2018.11.028.

[36] T.P. Heins, N. Schlüter, U. Schroder, Electrode-resolved monitoring of the ageing of large-scale lithium-ion cells by using electrochemical impedance spectroscopy, ChemElectroChem 4 (11) (2017) 2921 2927, https://doi.org/10.1002/celc.201700686.

[37] A.M. Colclasure, R.J. Kee, Thermodynamically consistent modeling of elementary electrochemistry in lithium-ion batteries, Electrochim. Acta 55 (2010) 8960 8973, https://doi.org/10.1016/j.electacta.2010.08.018.

[38] V. Laue, O. Schmidt, H. Dreger, X. Xie, F. Roder, R. Schenkendorf, A. Kwade, U. Krewer, Model-Based Uncertainty Quantification for the Product Properties of Lithium-Ion Batteries, Unpublished, doi:10.1002/ente.20.1900201.

[39] J. Vazquez-Arenas, L.E. Gimenez, M. Fowler, T. Han, S.K. Chen, A rapid estimation and sensitivity analysis of parameters describing the behavior of commercial Li-ion batteries including thermal analysis, Energy Convers. Manag. 87 (2014) 472 482, https://doi.org/10.1016/j.enconman.2014.06.076.

[40] D.C. López, G. Wozny, A. Flores-Tlacuahuac, R. Vasquez-Medrano, V.M. Zavala, A computational framework for identifiability and ill-conditioning analysis of lithium-ion battery models, Ind. Eng. Chem. Res. 55 (11) (2016) 3026 3042, https://doi.org/10.1021/acs.iecr.5b03910.

[41] H. Zheng, R. Yang, G. Liu, X. Song, V.S. Battaglia, Cooperation between active material, polymeric binder and conductive carbon additive in lithium ion battery cathode, J. Phys. Chem. 116 (7) (2012) 4875 4882, https://doi.org/10.1021/jp208428w.

[42] J. Marcicki, M. Canova, a. T. Conlisk, G. Rizzoni, Design and parametrization analysis of a reduced-order electrochemical model of graphite/LiFePO4 cells for SOC/SOH estimation, J. Power Sources 237 (2013) 310 324, https://doi.org/10.1016/j.jpowsour.2012.12.120.